

A comprehensive analysis of porous graphene-reinforced curved beams by finite element approach using higher-order structural theory: bending, vibration and buckling

B. Anirudh^a, M. Ganapathi^a, C. Anant^a, O. Polit^{b*}

^a *School of Mechanical Engineering, Vellore Institute of Technology, Vellore-632 014, India*

^b *LEME, UPL, Univ. Paris Nanterre, 50 rue de Sevres, 92410 Ville d'Avray, France*

Running title: Bending, vibration, buckling of porous graphene-reinforced curved beams

Acknowledgment

The authors did not receive support from any funding agencies and also confirm that they are not in any form of conflict of interest.

* Correspondence

E-mail: olivier.polit@parisnanterre.fr (O. Polit).

Highlights

- Static and dynamic study GPL reinforced curved beam by trigonometric shear deformation theory
- Inclusion of various form distributions for the pores and GPLs presence in the beam.
- Provided the results for different radii of curvature of beams and different boundary conditions.
- Conducted a thorough study considering various geometry and material parameters.
- Generated new results for benchmarking the solutions from other numerical/analytical approach.

A comprehensive analysis of porous graphene-reinforced curved beams by finite element approach using higher-order structural theory: bending, vibration and buckling

B. Anirudh^a, M. Ganapathi^a, C. Anant^a, O. Polit^{b*}

^a School of Mechanical Engineering, Vellore Institute of Technology, Vellore-632 014, India

^b LEME, UPL, Univ. Paris Nanterre, 50 rue de Sevres, 92410 Ville d'Avray, France

Summary

In this paper, the bending, vibration and buckling characteristics of functionally graded porous graphene-reinforced nanocomposite curved beams are studied based on a trigonometric shear deformation theory. The effect of various theories deduced from the proposed formulation on the static and dynamic behavior of curved nanocomposite beams is also studied. The governing equilibrium equations are formed by applying Lagrangian equations of motion coupled with the finite element approach employing a 3-noded C^1 continuous curved beam element. The methodology developed here is tested for problems having known solutions in the open literature. A detailed investigation involving various parameters such as coefficient of porosity, type of distribution pattern for the porosity and graphene platelets, radius of curvature of curved beam, length-to-thickness ratio, the platelet geometry, and boundary conditions on the static bending, free vibration and elastic stability behavior of nanocomposite curved beams is conducted. New results for certain boundary conditions of graphene reinforced curved beams are presented. Participation of various types of in-plane and transverse bending modes responsible for yielding the lowest critical buckling loads/natural frequencies are also highlighted.

Keywords: Higher-order theory; Finite element; Bending; Free vibration; Buckling; Porous curved beams; Graphene reinforcement.

*Correspondence

E-mail: olivier.polit@parisnanterre.fr (O. Polit).

1. Introduction

Advancements in manufacturing and material characterization techniques aid designers to create efficient designs by tailoring material properties. Advanced composites like porous composite materials and in particular, metal foams, are gaining prominence in the electronics and aerospace industries especially because of their lightweight, impact resistant and thermal resistant properties [1-4]. Metal foams can fall under the category of Functionally Graded Materials (FGM) as the size and density of porosity in metal foams can be varied directionally and have been realized in laboratories [5]. Since porous composite materials are lightweight and have low structural stiffness, the prediction of the mechanical behavior under different situations including the boundary conditions, loads and the reinforced-material inclusions like graphene platelets are warranted. The available appropriate studies are discussed in the subsequent paragraph.

Functionally graded porous straight beams and plates subjected to different environments were analyzed both theoretically and experimentally to characterize different mechanical behaviors [6-10]. To improve the structural stiffness, micro/nanofillers like Graphene Platelets (GPLs) can be introduced in the matrix. The global properties of the materials like strength and stiffness are governed by weight fraction and dispersion form of GPLs in the matrix given in Refs. [11-13]. The advantages of using GPLs or Carbon Nanotubes (CNTs) reinforcements to improve the vibrational and buckling behavior of beams, plates, and shells were dealt in Refs. [14-17]. Furthermore, the nonlinear vibrational characteristics of functionally graded CNT reinforced laminates were treated in Refs. [18-20]. Sandwich panels with CNT reinforced face sheets were analyzed for flutter study using a higher-order theory by Sankar et al. [21] and CNT reinforced shells were analyzed for post-buckling by Shen [22, 23].

The flexibility in making differently sized graphene platelets by using the lay-up of 2D form of graphite nano-crystals [24, 25] and the recent studies outlining the favorable characteristics of graphene platelet reinforce composites has led to an increase in their usage in many critical technologies. Buckling, post-buckling, bending and, stability analyses of GPL reinforced straight beams were carried out in [26,

27] and [28], respectively. An optimization study was also attempted in Ref. [29] discretely changing GPLs dispersion in the direction of thickness. The influence of GPLs on parametric instabilities and vibrational properties of beams were studied in Refs. [30, 31] and their impact on bending, vibration, dynamic impact response and thermal buckling of such plates were examined in [32-39]. Similar studies on GPL reinforced shells were also highlighted in Refs. [40-46].

A combination of porosity and GPLs in a metal matrix can help in achieving the desired strength and stiffness for a given weight of the structure. Work pertaining to such kind of composite structures available in the literature are discussed here. References [47-50] dealt with the vibrational behavior of porous GPL reinforced beams and Ref. [50], in particular, accounted for different distribution patterns as well. Some work done in literature pertaining to plate and shell structures were detailed in [51-53] where Yang et al. [51] employed the Chebyshev-Ritz discretization method to solve for free vibrational and buckling properties of plates, and finite element method was employed in Refs. [52,53] to solve the similar problems of shells.

Based on an extensive literature survey, it is evident that a large body of available research work on graphene-reinforced structures is limited to straight beams without the inclusion of pores in the metal/polymer matrix. Furthermore, all analyses have been carried out using the first-order or classic theory. Also, such studies pertaining to the curved beam are not commonly available in the literature, except the recent work of Polit et al. [54] which was focused on analytical approach considering bending analysis of simply supported case. [Comprehensive static and dynamic analyses of graphene reinforced curved beam considering different boundary conditions are scarce in the literature.](#) The present paper concerns itself with static, stability and free vibration behavior of GPL reinforced porous curved beams based on finite element approach introducing a trigonometric refined beam theory proposed by Polit et al. [55] and Touratier [56]. [Since the trigonometric refined theory used here is a class of higher-order theory, it can accurately predict the structural behavior for various types of nanocomposite curved beam with graphene reinforcement.](#) Lagrangian equations of motion are employed to develop the governing equations that are solved introducing the finite element procedure. [The formulation is validated against](#)

the available analytical methods. A detailed numerical experimentation is made varying the design parameters such as beam angle, geometry of GPL, beam thickness ratio, dispersion form of porosity and GPLs, and boundary conditions. Some new results are provided for various boundary conditions that can form benchmark solutions while applying other numerical or analytical approach to study such problems.

The structure of the paper is outlined as follows: Material part of porosity dispersion and GPL form are given in section 2, curved beam theory and governing equations in section 3, results and discussion in section 4, and followed by a conclusion.

2. Formulation of effective properties

The material considered here is a porous curved beam involving metal foam which is reinforced with graphene nanoplatelets. The porosity is presumed as closed-cells in nature and is distributed through the thickness in different patterns. The graphene platelet properties are governed by their geometric parameters and are also distributed through the thickness in different forms. The evaluation of the effective properties is briefly outlined here [54, 57-61].

2.1. Distribution of porosity

The material properties of a closed cell porous structure are presumed to change in the thickness plane as a function of z coordinate as indicated in Fig. 1. The effective mass density and Young's modulus are written as follows [6,50,53]

$$\begin{aligned}\rho(z) &= \hat{\rho}[1 - c_m\lambda(z)] \\ E(z) &= \hat{E}[1 - c_p\lambda(z)]\end{aligned}\tag{1}$$

where $\hat{\rho}$ & \hat{E} are the density and Young's modulus of nanocomposite curved beam, respectively, without having any defects like pores/porosity; c_m & c_p are porosity coefficients pertaining to density and stiffness functions, respectively. $\lambda(z)$ refers the porosity dispersion patterns that are selected here as uniform, symmetric and unsymmetric variations [6], as represented in Fig. 1a and is shown below as

$$\lambda(z) = \begin{cases} \lambda_0 \\ \cos\left(\frac{\pi z}{h}\right) \\ \cos\left(\frac{\pi z}{2h} + \pi/4\right) \end{cases} \quad (2)$$

The coefficient c_p related to the stiffness function given in Eq. (1) is treated as

$$c_p = 1 - \bar{E}_2/\bar{E}_1 \quad (3)$$

where \bar{E}_1 & \bar{E}_2 are the high and low values of Young's moduli of GPL reinforced curved beams with the presence of non-uniform porous dispersion, respectively. The constant c_p is considered to be one of the primary parameters for the design of such structures.

The relationship between the porosity coefficients c_p and c_m involved in Eq. (1) can be obtained using the curve fitting equation developed for $(E(z)/\hat{E})$ from the data generated by Gaussian Random Field model [62, 63] as

$$c_m = \frac{1.121 \left[1 - (1 - c_p \lambda(z))^{\frac{1}{2.3}} \right]}{\lambda(z)} \quad (4)$$

Similarly, the fitting data formed for the effective Poisson's ratio [63] is given as

$$\nu(z) = 0.221c_m\lambda(z) + \hat{\nu}(0.342 [c_m\lambda(z)]^2 - 1.21c_m\lambda(z) + 1) \quad (5)$$

To compute the λ_0 value of the uniform porosity distribution case, Eq. (2), it is assumed that the total weight of the beam is constant, irrespective of the variation in the porosity distribution. This allows one to find the value of λ_0 using a reference distribution such as the symmetric case, and by using Eq. (4) in the density equation Eq. (1) as

$$\lambda_0 = \frac{1}{c_p} \left[1 - \left(\frac{1/h \int_{-h/2}^{h/2} \rho(z)/\hat{\rho} dz + 0.121}{1.121} \right)^{2.3} \right] \quad (6)$$

With the above details, the equivalent material properties of the GPL reinforced matrix, considering the introduction of porosity in a GPL reinforced composite, can be found. To evaluate this, the beam can be first considered to be reinforced with GPLs, thus forming as pure nano-composites. The elastic modulus \bar{E} of such beam is estimated from the expression of the Halpin-Tsai data model [59] while the density $\hat{\rho}$ and Poisson's ratio $\hat{\nu}$ for the same case are found by using rule of mixtures as shown below.

$$\hat{E} = \frac{3}{8} \left(\frac{1 + \alpha_{gpl}^l \beta_{gpl}^l V_{gpl}}{1 - \beta_{gpl}^l V_{gpl}} \right) E_m + \frac{5}{8} \left(\frac{1 + \alpha_{gpl}^w \beta_{gpl}^w V_{gpl}}{1 - \beta_{gpl}^w V_{gpl}} \right) E_m \quad (7)$$

$$\hat{\rho} = \rho_{gpl} V_{gpl} + \rho_m V_m \quad (8)$$

$$\hat{\nu} = \nu_{gpl} V_{gpl} + \nu_m V_m \quad (9)$$

where $V_m = 1 - V_{gpl}$.

The material parameters V_{gpl} & V_m , respectively, denote the volume fractions of GPLs and matrix material presented in the resultant composite, respectively; ν_{gpl} & ν_m , ρ_{gpl} & ρ_m are the mass densities, Poisson's ratios of GPLs and matrix, respectively; E_m is the elastic modulus of the matrix. The geometry parameters of graphene platelet ($\alpha_{gpl}^l, \alpha_{gpl}^w$) can be written in terms of GPL thickness and aspect ratios; $\beta_{gpl}^l, \beta_{gpl}^w$ are related to the elastic modulus ratio of GPL and matrix, and GPL geometric parameters, respectively as

$$\alpha_{gpl}^l = \frac{2l_{gpl}}{t_{gpl}}; \alpha_{gpl}^w = \frac{2w_{gpl}}{t_{gpl}} \quad (10a)$$

$$\beta_{gpl}^l = \frac{(E_{gpl}/E_m)^{-1}}{(E_{gpl}/E_m)^{-1} - \alpha_{gpl}^l}; \beta_{gpl}^w = \frac{(E_{gpl}/E_m)^{-1}}{(E_{gpl}/E_m)^{-1} + \alpha_{gpl}^w} \quad (10b)$$

Here, t_{gpl}, w_{gpl} & l_{gpl} are the GPL thickness, breath, and length, respectively; E_{gpl} is the elastic modulus of the GPL fillers.

2.2. GPL distribution

The volume fraction V_{gpl} in Eq. (11) is changed in the thickness direction assuming various dispersion forms (uniform, symmetric and unsymmetric cases) as shown in Fig. 1b and can be stated as

$$V_{gpl} = \begin{cases} V_1^j \\ V_2^j [1 - \cos(\pi z/h)] \\ V_3^j \left[1 - \cos\left(\frac{\pi z}{2h} + \pi/4\right) \right] \end{cases} \quad (11)$$

where the superscript j indicates the dispersion pattern of porosity.

The volume fraction V_{gpl} , in general, can be linked with the GPL weight fraction (W_{gpl}) as

$$V_{gpl} = \frac{W_{gpl}}{W_{gpl} + \rho_{gpl}/\rho_m(1 - W_{gpl})} \quad (12)$$

The maximum value V_i in Eq. (11) can be computed using Eqs. (11), (12) in conjunction with the relative weights calculated from Eq. (1) for the selected porosity and GPL distributions as

$$\int_{-h/2}^{h/2} V_{gpl} [1 - e_m \chi(z)] dz = \frac{W_{gpl}}{[W_{gpl} + (\rho_{gpl}/\rho_m)(1 - W_{gpl})]} \int_{-h/2}^{h/2} [1 - e_m \chi(z)] dz \quad (13)$$

3. Structural Formulation

The beam model considered here is based on a curved one with length L , thickness h , unit width, and radius of curvature R having beam included angle ϕ , as illustrated in Fig. 2a. The structural behavior is defined following a trigonometric shear deformation theory that utilizes a sinusoidal function in representing the deformation of the beam cross-section, referred as the SIN model [54-56]. The displacements in the x direction along the length and $z \in (-\frac{h}{2}, \frac{h}{2})$ direction i.e the thickness direction, are represented by u and w respectively and are related to the field variables as follows

$$\begin{cases} u_1(x, z, t) = \left(1 + \frac{z}{R}\right) u_0(x, t) - z w'_0(x, t) + \Gamma(z) \gamma_0(x, t) \\ u_3(x, z, t) = w_0(x, t) \end{cases} \quad (14)$$

where t is the time, and the transverse shear strain contribution γ_0 can be given as

$$\gamma_0(x, t) = \theta(x, t) + w'_0(x, t) - \frac{1}{R} v_0(x, t) \quad (15)$$

The kinematics assumed here has three field variables as functions of x and t , independent of the thickness direction; u_0 is the curvilinear axial displacement; w_0 is the transverse displacement along the beam neural axis; θ is the rotation of the cross-section. Derivatives are denoted by $(\cdot)' = \partial/\partial x$ and $(\cdot)^\cdot = \partial/\partial t$. The function $\Gamma(z)$ in Eq. (14) is used to deduce different theories, for instance, the classical Euler Bernoulli theory by $\Gamma(z) = 0$, Timoshenko theory by $\Gamma(z) = z$, and or the SIN theory by $\Gamma(z) = \frac{h}{\pi} \sin \frac{\pi z}{h}$.

The strains obtained from kinematic equations and the relation between these strains with stresses by the constitutive law are stated as follows

$$\begin{Bmatrix} \varepsilon_{11} \\ \varepsilon_{33} \\ \gamma_{13} \end{Bmatrix} = \begin{Bmatrix} v_0' + \frac{w_0}{R} + z \left(\frac{v_0'}{R} - w_0'' \right) + \Gamma(z) \gamma_0' \\ 0 \\ \Gamma'(z) \gamma_0 \end{Bmatrix} \quad (16)$$

$$\begin{Bmatrix} \sigma_{11} \\ \sigma_{13} \end{Bmatrix} = \begin{Bmatrix} C_{11} \varepsilon_{11} \\ C_{66} \gamma_{13} \end{Bmatrix} \quad (17)$$

where $C_{11} = \frac{E}{1-\nu^2}$; $C_{66} = G$

For the material model considered here, the shear modulus G can be connected to the Young's modulus E by $E = 2G(1 + \nu)$.

The porous GPL curved beam is supposed to be under an externally distributed force $P_3(x, t)$ acting on the top of the beam ($z = h/2$) whereas the in-plane compressive force $P_0(x, t)$ is assumed to be present in the tangent direction along the mid-line of the beam *i.e.* such in-plane load may form when the curved beam is under uniform pressure [66, 67]. The equations of motion are in general developed through the Lagrangian equations of motion by

$$\frac{d}{dt} \left[\frac{\partial(T-U_T)}{\partial \delta_i} \right] - \left[\frac{\partial(T-U_T)}{\partial \delta_i} \right] = 0, i = 1, 2, \dots, n \quad (18)$$

where, δ_i is the vector of global degrees of freedom; U_T is the total energy consisting of strain energy (U_s), the potential energy by the compressive axial force $P_0(V)$ and work done by the externally applied pressure load $P_3(W)$; T is the kinetic energy. All these energy contributions can be expressed as

$$U_s(\delta) = \int_0^L \int_{-\frac{h}{2}}^{\frac{h}{2}} (\delta \varepsilon^T \sigma) dz dx = \frac{1}{2} [\delta]^T [K] [\delta] \quad (19a)$$

$$W(\delta) = - \int_0^L P_3 w dx \quad (19b)$$

$$V(\delta) = - \frac{1}{2} \int_0^L \int_{-h/2}^{h/2} P_0 \left(\frac{\partial w}{\partial x} - \frac{u_0}{R} \right)^2 = \frac{1}{2} \{\delta\}^T [K_G] \{\delta\} \quad (19c)$$

$$T(\delta) = \frac{1}{2} \int_0^L \int_{-\frac{h}{2}}^{\frac{h}{2}} \rho \{\dot{u} \dot{w}\} \{\dot{u} \dot{w}\}^T dx dz = \frac{1}{2} [\dot{\delta}]^T [M] [\dot{\delta}] \quad (19d)$$

where $[M]$ & $[K]$ are the matrices of global mass and stiffness, respectively. $[K_G]$ is the matrix of global geometric stiffness.

Substituting Eqs (19) in Lagrange's equation of motion (18), the following governing equations for various problems such as bending, vibration, and buckling identified are outlined as

$$\begin{aligned}
 [K]\{\delta\} &= \{F\} && \text{(bending)} \\
 ([K] - \omega^2[M])\{\delta\} &= \{0\} && \text{(free vibration)} \\
 ([K] - P_0[K_G])\{\delta\} &= \{0\} && \text{(buckling)} \tag{20}
 \end{aligned}$$

The different matrices involved in the above governing equations can be developed using finite element procedure. In the present work, a C^1 continuous 3-noded beam element with Hermite shape function for the transverse displacement function, w_0 and a quadratic function for axial displacement u_0 and cross-sectional rotation θ is proposed to study the problems [55]. The end nodes have 4 degrees of freedom (DoF) i.e. u_0 , w_0 , $w_{0,x}$ and θ , while the mid-node has 2 DoFs i.e. u_0 and θ , as depicted in Fig. 2b. The interpolation functions selected here interpolate the membrane/ shear strain energy term in a field-consistency way to avoid the membrane/shear locking syndrome. All the energy terms were numerically calculated adopting full integration. This element performs very well for thick/thin curved beam case. It has no artificial mode and produces the correct rigid body modes. The convergence characteristics of the element are good.

4. Numerical results and Discussion

4.1 The problems detailed

Here, the ability of the developed finite element formulation based on the trigonometric shear deformation theory using sine function as outlined in the previous section is tested for the known problems available in the open literature. A comprehensive study is carried out assuming parameters like

length-to-thickness ratio i.e. $S = L/h$, radius of curvature of curved beam R and beam angle ϕ , GPLs distribution and pores dispersion in the thickness direction, and GPL's geometry on the bending, buckling and vibration characteristics of GPL reinforced porous curved composite beams.

The beam geometry considered here consists of various types of curved beams including the straight one and fixing the length $L = 10\text{m}$. The curved beam angle $\phi = \{15^\circ, 60^\circ, 120^\circ\}$ is varied to represent the shallow/deep curved beam cases. The radius of curvature R can be computed from the relation, $L = R \times \phi$. For thin and thick beams, different values for $S = \{5, 10, 20\}$ are presumed.

Boundary Conditions: The following boundary conditions have been employed for the purpose of this study:

- movable simply supported (HH-movable): $w_0 = 0$ at $x = 0, L$
- immovable simply supported (HH-immovable): $u_0 = w_0 = 0$ at $x = 0, L$
- fully clamped support (CC): $u_0 = \theta = w_0 = w_0' = 0$ at $x = 0, L$
- clamped-hinged support (CH): $u_0 = \theta = w_0 = w_0' = 0$ at $x = 0$; $u_0 = w_0 = 0$ at $x = L$

The properties of GPLs and metal matrix are taken as [64,65]

- material: Young's modulus, $E_{gpl}=1.01$ TPa; density, $\rho_{gpl}= 1062.5$ kg/m³; Poisson's ratio, $\nu_{gpl}=0.186$
- geometry: width, $w_{gpl}=1.5$ μm , length, $l_{gpl}=2.5$ μm , thickness, $t_{gpl}=1.5$ nm,
- metal matrix: Copper based metal- Young's modulus $E_m=130$ GPa; density, $\rho_m= 8960$ kg/m³; Poisson's ratio, $\nu_m=0.34$

Results: All results presented here, unless mentioned otherwise, the following non-dimensional forms are introduced as

- bending: $\bar{w} = w \frac{100E_m I}{p_3 L^4}$; $\bar{\sigma}_{11} = 10 \sigma_{11} \frac{h^2}{p_3 L^2}$; $\bar{\sigma}_{13} = 100 \sigma_{13} \frac{h^2}{p_3 L^2}$
- buckling: $P_{cr} = P_0 \frac{L^2}{E_m I}$

- vibration: $\bar{\omega} = \omega L^2 \sqrt{\frac{m}{E_m I}}$; where $m = \rho h$ and $I = h^3/12$

4.2 Assessment of present model

Based on the progressive mesh refinement, a 32-elements discretization model was found to yield the required converged solutions for different boundary conditions and for all the analyses focused in the present study as seen from Table 1. Before conducting in-depth analyses, the performance of the model was assessed by comparing against existing results in the tabular or graphical form for isotropic curved beams, and graphene-reinforced straight beam cases. Tables 2-4 highlight the comparison of the present results with those of analytical solutions for the static bending/buckling/ free vibrations of hinged-hinged isotropic curved beams. They are found to be in very good agreement. As there is no work seen in the literature related to static/dynamic study of graphene-reinforced metal or polymer beams, the available analytical solutions for straight beam with such reinforcement are compared with the obtained results using the present model in Figs. 3-5, respectively for the static, buckling and free vibration cases. It is noticed from Figs. 3-5 that the present numerical solutions are in excellent agreement with those of the available analytical methods.

4.3. Bending analysis

The curved beams with ($L/h = 5, 10$ & $\phi = 45^\circ$) are subjected to uniformly distributed load of magnitude $P_3 \left(x, z = \frac{h}{2} \right) = p_3 \sin \frac{\pi x}{L}$ in the transverse direction. The GPL weight fraction and the porosity coefficient are assumed as $W_{gpl} = 1\%$ and $c_p = 0.5$. Considering three different types of dispersion for porosity and GPLs in the beam as shown in Fig. 1, the maximum nondimensional displacements of beams evaluated for different boundary conditions are shown in Table 5 along with those of straight beam cases. It is seen that, in general, the combination of a symmetric GPL and symmetric porosity distribution yields the lowest deflection values, thus exhibiting maximum stiffness, next followed by the uniform and unsymmetric distribution cases, respectively. The high bending stiffness in symmetric distribution case is attributed to the high concentration of GPL and less pores near the upper and lower surfaces of the beam

compared to those of around midplane values. It is further viewed that the influence of GPL distribution shows significant change in the stiffness for all cases in comparison with those of porosity distributions. Also, the effect of radius of curvature of the beam is observed to noticeably reduce the nondimensional deflection, irrespective of material and geometric parameters because of the presence of coupling between bending and stretching in the curved beam. The clamped case gives lower deflection compared to all other supports, as expected. The deflection clamped-hinged beam falls in between the clamped-clamped and hinged-hinged case as expected. The detailed investigations, unless otherwise mentioned, are conducted by assuming symmetric distributions for the porosity and GPLs in the curved beams.

Next, the influence of the graphene platelets in the porous nanocomposite curved beam under uniform load on the bending deflection while varying the beam included angle $\phi = \{15^\circ, 60^\circ, 120^\circ\}$, the length-to-thickness ratio, $S \{5, 10, 20\}$ and boundary conditions is investigated and the results are depicted in Fig. 6. It can be opined from this figure that the beam bending stiffness increases significantly by dispersing the GPLs and, an addition of 1% weight fraction of GPLs results in about 45% decrease in maximum beam deflection for all boundary conditions considered here. Furthermore, the resistance of the beam against transverse load increases while increasing the beam included angle, and the boundary condition significantly affects the deflection. A gradual decrease in deflection is also noticed when increasing the percentage of weight fraction of GPL.

The through-thickness plots of shear and normal stresses (σ_{13} , σ_{11}) of porous GPL-reinforced curved beam having $\phi = 60^\circ$ & $S=5$ are presented in Fig. 7 for different boundary conditions assuming some values for GPL weight fraction and porosity coefficient ($c_p = 0.5$; $W_{gpl}=1\%$). The effect of different types of distributions for GPLs and porosity are also considered. It is noticed from this figure that the present model exhibits zero transverse shear stress values at the extreme surfaces of the curved beam as required. It is also observed that the variation of pores through the thickness has less effect compared to the influence of GPLs dispersion. Furthermore, the location of maximum shear stress value in the thickness direction can be different from the physical neutral axis and it is highly dependent on the GPLs

dispersion and pores distribution. This is due to the stiffness variation in the thickness direction. Also, it is seen that, for the clamped case, the transverse shear stress variation in the thickness direction is noticeably high when comparing with those of other boundary conditions. The variation of normal stress σ_{11} in direction of the thickness is nonlinear and the degree of nonlinearity is significantly influenced by the distribution of GPLs and pores. The location of zero normal stress σ_{11} value can be different from neutral axis as seen in the case of the location of the maximum shear stress in the thickness direction. However, the influence of boundary conditions on variation of normal stress through the thickness is less.

Next, the influence of aspect and thickness ratios (ℓ/w , ℓ/t) of graphene platelets on the bending behavior is examined assuming the curved porous beam with $\phi = 90^\circ$ & $L/h=5$, and symmetric dispersion for both GPLs and pores. The numerical results obtained are plotted in Fig.8 and it is evident that beams with graphene platelets with low aspect ratio and high thickness ratio have predominantly high beam stiffness, irrespective of the boundary conditions.

4.4. Buckling analysis

The elastic buckling study of porous graphene-reinforced curved beam ($c_p=0.5$ & $W_{gpl}=1\%$) is investigated by various types of dispersion of porosity/GPL in the reinforced metal matrix. The minimum critical buckling compressive load is presented in Table 6 for thick curved beams ($L/h = 5, 10$ & $\phi = 45^\circ$) including the straight beam case. Similar to the static bending study, it is seen that the symmetric pattern for both GPLs and porosity offers the maximum stiffness, thus yielding in high critical values. It is also seen that the critical buckling load increases significantly while increasing in thickness ratio of the beam and this is due to the involvement of higher mode corresponding to the lowest critical load.

Next, the buckling loads corresponding to the lowest buckling modes are evaluated for various thickness ratio values ($L/h=5, 10, 20$) and curved beam angle ($\phi = 15^\circ, 60^\circ, 120^\circ$) are detailed in Figs. 9. This Figure also brings out the effect of various boundary types on the buckling loads. The buckling mode plots with reference to transverse displacement and in-plane displacements (w , u_0) for hinged-

hinged and clamped are described in Fig. 10. From Fig. 9, it is observed that, for the shallow beam case, the critical buckling value is less compared to the cases of fairly deep and very deep beams. It is possibly due to the low membrane energy contribution to the total potential energy which increases with the beam included angle cases. However, for the hinged-hinged case, the total potential energy for the intermediate curved beam case $\phi = 60^\circ$ appears to be more compared to the case of deep beam ($\phi = 120^\circ$). Accordingly, the critical buckling value is somewhat more for fairly deep beam case ($\phi = 60^\circ$), irrespective of thickness ratio. But this trend is reversed in the case of clamped beam case, thus yielding higher buckling load for deep beam $\phi = 120^\circ$. This is attributed to the energy contribution due to the membrane and bending deformations. It is also viewed from Fig. 10 that, for the shallow curved beam, the lowest mode w for buckling mode matches the first symmetric mode whereas the first anti-symmetric mode w dominates the lowest critical load for the deep cases. It is also inferred that the enhancement in the compressive resisting load is noticeable while adding 1% GPLs in the metal matrix. It is further opined that the increase in the minimum critical compressive value is about 80% depending on the thickness ratio of the beam. It can be in general opined that the lowest buckling value for the selected curved beam depends on the participation of the type mode, symmetric or anti-symmetric mode, and also the boundary conditions.

4.5. Free vibration analyses

The free vibration study of the GPLs reinforced nanocomposite porous curved beams is investigated assuming symmetric dispersion for GPL and pores in the thickness direction based on the bending and buckling analyses. The detailed parametric investigation is made considering nanocomposite beams with $S=5, 10, 20$ and beam angle $\phi = 15^\circ, 60^\circ, 120^\circ$. The results for the fundamental frequency are plotted in Figs. 11. It is noticed from Fig. 11 that the fundamental frequency value for very deep beam case is higher for thick beam compared to the cases of shallow and fairly deep cases but it may change with the increase in thickness ratio and boundary condition as seen in Fig. 11. This behavior is qualitatively similar to those of buckling case. The vibration mode shapes with respect to transverse and

in-plane displacements (w, u_0) for hinged-hinged and clamped are shown in Fig. 12. It is viewed from this figure that the in-plane vibration modes are in general different from the buckling modes (Fig.10).

5. Conclusion

The application of finite element approach coupled with higher-order SIN model is carried out for bending, buckling and free vibration of graphene platelets reinforced porous curved beams. The performance of the numerical model is compared with the analytical method. A comprehensive analysis is done to highlight the effect of different design parameters like length-to-thickness ratio and boundary conditions, included angle of curved beam on the static and dynamic behavior of curved beams. From the present investigation, certain observations made are as follows:

- (i) The type of weight distribution of GPLs influences the beam stiffness considerably while comparing with the pores distribution pattern in the metal matrix.
- (ii) The increase in beam included angle decreases the deflection of the curved beam.
- (iii) The transverse shear stress variation in the thickness direction is noticeably high for the clamped case.
- (iv) The change in the normal stress in the thickness direction is nonlinear and the degree of nonlinearity depends on the distribution of GPLs and pores.
- (v) The occurrence of the maximum shear stress values and zero normal stress in the thickness direction is dependent on the dispersion type of pores and GPLs in the matrix.
- (vi) Graphene platelet geometric parameters significantly affect the structural design of the nanocomposite curved beam.
- (vii) Significant enhancement in the buckling value is observed while increasing GPLs weight fraction in comparison with the reduction level of static bending deflection of the beam.
- (viii) The buckling value of a curved beam significantly depends on the beam included angle.

- (ix) The increment in frequency value highly depends on the shallowness and thickness ratio of the reinforced porous curved beam.
- (x) The in-plane mode significantly affects the critical buckling and fundamental frequency values depending on the curved beam included angle.
- (xi) The results provided for certain boundary conditions can thus form as benchmark solutions while dealing with different theories/solution approaches.

References

1. Banhart J. Manufacture, characterisation and application of cellular metals and metal foams. *Prog Mater Sci* 2001;46:559–632.
2. Qin J, Chen Q, Yang C, Huang Y. Research process on property and application of metal porous materials. *J Alloys Compd* 2016;654:39–44.
3. Ashby MF, Evans T, Fleck NA, Hutchinson JW, Wadley HNG, Gibson LJ. Metal foams: a design guide. Butterworth-Heinemann, Oxford, UK. *Mater Des*; 2002;23(1):119.
4. Lefebvre L-P, Banhart J, Dunand DC. Porous metals and metallic foams: current status and recent developments. *Adv Eng Mater* 2008;10:775–87.
5. Pollien A, Conde Y, Pambaguian L, Mortensen A. Graded open-cell aluminium foam core sandwich beams. *Mater Sci Eng A* 2005;404:9–18.
6. Chen D, Yang J, Kitipornchai S. Elastic buckling and static bending of shear deformable functionally graded porous beam. *Compos Struct* 2015;133:54–61.
7. Wu D, Liu A, Huang Y, Huang Y, Pi Y, Gao W. Dynamic analysis of functionally graded porous structures through finite element analysis. *Eng Struct* 2018;165:287–301.
8. Chen D, Kitipornchai S, Yang J. Nonlinear free vibration of shear deformable sandwich beam with a functionally graded porous core. *Thin-Walled Struct* 2016;107:39–48.
9. Jing L, Wang Z, Ning J, Zhao L. The dynamic response of sandwich beams with open-cell metal foam cores. *Compos Part B Eng* 2011;42:1–10.
10. Cong PH, Chien TM, Khoa ND, Duc ND. Nonlinear thermomechanical buckling and post-buckling response of porous FGM plates using Reddy's HSDT. *Aerosp Sci Technol* 2018;77:419–28.
11. Li Z, Young RJ, Wilson NR, Kinloch IA, Vallés C, Li Z. Effect of the orientation of graphene-based nanoplatelets upon the Young's modulus of nanocomposites. *Compos Sci Technol* 2016;123:125–33.

12. Atif R, Shyha I, Inam F. Mechanical, Thermal, and Electrical Properties of Graphene-Epoxy Nanocomposites—A Review. *Polymers (Basel)* 2016;8(8):28.
13. Mittal G, Dhand V, Rhee KY, Park S-J, Lee WR. A review on carbon nanotubes and graphene as fillers in reinforced polymer nanocomposites. *J Ind Eng Chem* 2015;21:11–25.
14. Wu H, Kitipornchai S, Yang J. Imperfection sensitivity of thermal post-buckling behaviour of functionally graded carbon nanotube-reinforced composite beams. *Appl Math Model* 2017;42:735–52.
15. Heshmati M, Yas MH, Daneshmand F. A comprehensive study on the vibrational behavior of CNT-reinforced composite beams. *Compos Struct* 2015;125:434–48.
16. Deepak BP, Ganguli R, Gopalakrishnan S. Dynamics of rotating composite beams: A comparative study between CNT reinforced polymer composite beams and laminated composite beams using spectral finite elements. *Int J Mech Sci* 2012;64:110–26.
17. Zhu P, Lei ZX, Liew KM. Static and free vibration analyses of carbon nanotube-reinforced composite plates using finite element method with first order shear deformation plate theory. *Compos Struct* 2012;94:1450–60.
18. Lei ZX, Liew KM, Yu JL. Free vibration analysis of functionally graded carbon nanotube-reinforced composite plates using the element-free kp-Ritz method in thermal environment. *Compos Struct* 2013;106:128–38.
19. Wang Z-X, Shen H-S. Nonlinear vibration of nanotube-reinforced composite plates in thermal environments. *Comput Mater Sci* 2011;50:2319–30.
20. Wang Z-X, Shen H-S. Nonlinear vibration and bending of sandwich plates with nanotube-reinforced composite face sheets. *Compos Part B Eng* 2012;43:411–21.
21. Sankar A, Natarajan S, Zineb T Ben, Ganapathi M. Investigation of supersonic flutter of thick doubly curved sandwich panels with CNT reinforced facesheets using higher-order structural theory. *Compos Struct* 2015;127:340–55.

22. Shen H-S. Postbuckling of nanotube-reinforced composite cylindrical shells in thermal environments, Part I: Axially-loaded shells. *Compos Struct* 2011;93:2096–108.
23. Shen H-S. Postbuckling of nanotube-reinforced composite cylindrical shells in thermal environments, Part II: Pressure-loaded shells. *Compos Struct* 2011;93:2496–503.
24. Gong, L, Young RJ, Kinloch IA, Riaz I, Jalil R, Novoselov KS. Optimizing the reinforcement of polymer-based nanocomposites by graphene, *ACS Nano* 2012;6:2086–95.
25. García-Macías E, Rodríguez-Tembleque L, Sdáz A. Bending and free vibration analysis of functionally graded graphene vs. carbon nanotube reinforced composite plates. *Compos Struct* 2018;186:123–38.
26. Zhang Z, Li Y, Wu H, Zhang H, Wu H, Jiang S, et al. Mechanical analysis of functionally graded graphene oxide-reinforced composite beams based on the first-order shear deformation theory. *Mech Adv Mater Struct* 2018:251–9.
<https://doi.org/10.1080/15376494.2018.1444216>
27. Yang J, Wu H, Kitipornchai S. Buckling and postbuckling of functionally graded multilayer graphene platelet-reinforced composite beams. *Compos Struct* 2017;161:111–8.
28. Shen H-S, Lin F, Xiang Y. Nonlinear bending and thermal postbuckling of functionally graded graphene-reinforced composite laminated beams resting on elastic foundations. *Eng Struct* 2017;140:89–97.
29. Kiani Y, Mirzaei M. Enhancement of non-linear thermal stability of temperature dependent laminated beams with graphene reinforcements. *Compos Struct* 2018;186:114–22.
30. Wu H, Yang J, Kitipornchai S. Dynamic instability of functionally graded multilayer graphene nanocomposite beams in thermal environment. *Compos Struct* 2017;162:244–54.
31. Shen H-S, Lin F, Xiang Y. Nonlinear vibration of functionally graded graphene-reinforced composite laminated beams resting on elastic foundations in thermal environments. *Nonlinear Dyn* 2017;90:899–914.

32. Song M, Yang J, Kitipornchai S. Bending and buckling analyses of functionally graded polymer composite plates reinforced with graphene nanoplatelets. *Compos Part B Eng* 2018;134:106–13.
33. Song M, Kitipornchai S, Yang J. Free and forced vibrations of functionally graded polymer composite plates reinforced with graphene nanoplatelets. *Compos Struct* 2017;159:579–88.
34. Fan Y, Xiang Y, Shen H-S, Hui D. Nonlinear low-velocity impact response of FG-GRC laminated plates resting on visco-elastic foundations. *Compos Part B Eng* 2018;144:184–94.
35. Lei Z, Su Q, Zeng H, Zhang Y, Yu C. Parametric studies on buckling behavior of functionally graded graphene-reinforced composites laminated plates in thermal environment. *Compos Struct*;2018:In-press.(Available Online).
<https://doi.org/10.1016/j.compstruct.2018.03.079>
36. Wu H, Kitipornchai S, Yang J. Thermal buckling and postbuckling of functionally graded graphene nanocomposite plates. *Mater Des* 2017;132:430–41.
37. Shen H-S, Xiang Y, Lin F, Hui D. Buckling and postbuckling of functionally graded graphene-reinforced composite laminated plates in thermal environments. *Compos Part B Eng* 2017;119:67–78.
38. Shen H-S, Xiang Y, Lin F. Thermal buckling and postbuckling of functionally graded graphene-reinforced composite laminated plates resting on elastic foundations. *Thin-Walled Struct* 2017;118:229–37.
39. Shen H-S, Lin F, Xiang Y. Nonlinear vibration of functionally graded graphene-reinforced composite laminated beams resting on elastic foundations in thermal environments. *Nonlinear Dyn* 2017;90:899–914.
40. Liu D, Kitipornchai S, Chen W, Yang J. Three-dimensional buckling and free vibration analyses of initially stressed functionally graded graphene reinforced composite cylindrical shell. *Compos Struct* 2018;189:560–9.

41. Wang A, Chen H, Hao Y, Zhang W. Vibration and bending behavior of functionally graded nanocomposite doubly-curved shallow shells reinforced by graphene nanoplatelets. *Results Phys* 2018;9:550–9.
42. Wang Y, Feng C, Zhao Z, Yang J. Eigenvalue buckling of functionally graded cylindrical shells reinforced with graphene platelets (GPL). *Compos Struct*;2017: In-press. (Available Online) <https://doi.org/10.1016/j.compstruct.2017.10.005>
43. Wang Y, Feng C, Zhao Z, Yang J. Buckling of Graphene Platelet Reinforced Composite Cylindrical Shell with Cutout. *Int J Struct Stab Dyn* 2018;18:1850040.
44. Shen H-S, Xiang Y, Fan Y, Hui D. Nonlinear bending analysis of FG-GRC laminated cylindrical panels on elastic foundations in thermal environments. *Compos Part B Eng* 2018;141:148–57.
45. Shen H-S, Xiang Y, Fan Y. Postbuckling of functionally graded graphene-reinforced composite laminated cylindrical panels under axial compression in thermal environments. *Int J Mech Sci* 2018;135:398–409.
46. Shen H-S, Xiang Y. Postbuckling of functionally graded graphene-reinforced composite laminated cylindrical shells subjected to external pressure in thermal environments. *Thin-Walled Struct* 2018;124:151–60.
47. Barati MR, Zenkour AM. Analysis of postbuckling of graded porous GPL-reinforced beams with geometrical imperfection. *Mech Adv Mater Struct* 2018:1–9. <https://doi.org/10.1080/15376494.2017.1400622>
48. Barati MR, Zenkour AM. Post-buckling analysis of refined shear deformable graphene platelet reinforced beams with porosities and geometrical imperfection. *Compos Struct* 2017;181:194–202.
49. Chen D, Yang J, Kitipornchai S. Nonlinear vibration and postbuckling of functionally graded graphene reinforced porous nanocomposite beams. *Compos Sci Technol* 2017;142:235–45.

50. Kitipornchai S, Chen D, Yang J. Free vibration and elastic buckling of functionally graded porous beams reinforced by graphene platelets. *Mater Des* 2017;116:656–65.
51. Yang J, Chen D, Kitipornchai S. Buckling and free vibration analyses of functionally graded graphene reinforced porous nanocomposite plates based on Chebyshev-Ritz method. *Compos Struct* 2018;193:281–94.
52. Barati MR, Zenkour AM. Vibration analysis of functionally graded graphene platelet reinforced cylindrical shells with different porosity distributions. *Mech Adv Mater Struct* 2018:1–9. <https://doi.org/10.1080/15376494.2018.1444235>
53. Dong YH, Li YH, Chen D, Yang J. Vibration characteristics of functionally graded graphene reinforced porous nanocomposite cylindrical shells with spinning motion. *Compos Part B Eng* 2018;145:1–13.
54. Polit O, Anant C, Anirudh B, Ganapathi M. Functionally graded graphene reinforced porous nanocomposite curved beams: Bending and elastic stability using a higher-order model with thickness stretch effect. *Compos Part B Eng* 2018;166:310–27. <https://doi.org/10.1016/j.compositesb.2018.11.074>.
55. Polit O, Merzouki T, Ganapathi M. Elastic stability of curved nanobeam based on higher-order shear deformation theory and nonlocal analysis by finite element approach. *Finite Elem Anal Des* 2018;146:1–15. doi:10.1016/j.finel.2018.04.002.
56. Touratier M. An efficient standard plate theory. *Int J Eng Sci* 1991;29:901–16.
57. Liu F, Ming P, Li J. Ab initio calculation of ideal strength and phonon instability of graphene under tension. *Phys. Rev. B* 2007;76: 064120.
58. Shokrieh M, Esmkhani M, Shokrieh Z, Zhao Z. Stiffness prediction of graphene nanoplatelet/epoxy nanocomposites by a combined molecular dynamics–micromechanics method, *Comput. Mater. Sci.* 2014;92: 444–450.
59. Afdl J., Kardos J., The Halpin-Tsai equation: a review. *Polym. Eng. Sci.* 1976;16: 344–352.

60. Rafiee M A, Rafiee J, Wang Z, Song H, Yu Z -Z, Koratkar N. Enhanced mechanical properties of nanocomposites at low graphene content. *ACS Nano* 2009;3: 3884–3890.
61. De Villoria R G, Miravete A, Mechanical model to evaluate the effect of the dispersion in nanocomposites, *Acta Mater.* 2007;55: 3025–3031.
62. Roberts A, Garboczi E. Elastic moduli of model random three-dimensional closed-cell cellular solids. *Acta Mater* 2001;49:189–197.
63. Roberts A, Gaboczi E. Computation of linear elastic properties of random porous materials with a wide variety of microstructure. *Proceeding R. Soc. London A.*2002;458:1033-54.
64. Luu A-T, Lim N-I, Lee J. Bending and buckling of general laminated curved beams using nurbs-based isogeometric analysis. *Eur. J. Mech. Solids.* 2015;54:218-31.
65. Timoshenko S, Gere J. *Theory of elastic stability.* 2nd Edition, McGraw-Hill, New-York, 1961.
66. Hosseini S A H, Rahmani O. Free Vibration of shallow and deep Curved FG Nanobeam via nonlocal Timoshenko curved beam model. *Applied Physics A* 2016;122: 1-11.
67. Ganapathi M, Polit O. A nonlocal higher-order model including thickness stretching effect for bending and buckling of curved nanobeams. *Applied Math. Model* 2018; 57: 121-141.
68. Kang K J, Bert C W, Striz A G. Vibration and buckling analysis of circular arches using DQM. *Comp Struct* 1996;60:49–57.

Legends for Tables

Table 1. Mesh convergence table for different loading and boundary conditions, C - C and H - H-movable ($L/h=5$, $\phi = 60^\circ$, $c_p = 0.5$, $W_{gpl} = 1\%$).

Table 2. Comparison of nondimensional deflections (\bar{u}_3) for different L/h , beam angles (ϕ), and theories ($c_p = 0$, $W_{gpl} = 0\%$).

Table 3. Comparison of non-dimensional first, second and third fundamental frequencies of curved isotropic beam (H - H-movable boundary condition, $\phi = 60^\circ$).

Table 4. Critical buckling load, \bar{P}_{cr} , of an isotropic curved beam (H - H-movable)

Table 5. Non-dimensional deflection (\bar{u}_3) of curved beams of different porosity and GPLs weight distribution types for different boundary conditions ($c_p = 0.5$, $W_{gpl} = 1\%$).

Table 6. Non-dimensional buckling load, \bar{P}_{cr} of different porosity and GPLs weight distribution types for different boundary conditions ($c_p = 0.5$, $W_{gpl} = 1\%$).

Legends for Figures

Figure 1. Distribution of porosity and GPLs in the thickness direction: (a) Porosity; (b) GPLs.

Figure 2. a) Geometrical parameters of curved beam; b) Beam element with the degrees of freedom.

Figure 3. Comparison of non - dimensional deflections against porosity coefficient for the straight nanocomposite beam under uniform load for different boundary conditions ($L/h = 20$, $W_{gpl} = 0\%$).

Figure 4. Comparison of critical buckling load increment of straight GPL reinforced beam against weight fraction of GPL for different values for porosity coefficient and different GPL distributions (CC boundary condition, $L/h=20$, symmetric porosity distribution).

Figure 5. Comparison of fundamental frequency increment of straight GPL reinforced beam against GPL weight fraction of GPLs for different GPL distributions and boundary conditions ($c_p = 0.5$, $L/h = 20$, symmetric porosity distribution).

Figure 6. Non - dimensional deflections of curved beams with different beam angles (ϕ) against GPL weight fraction (W_{gpl}) for different thickness ratios and different boundary conditions ($c_p = 0.5$, symmetric distribution type for porosity and GPLs).

Figure 7. Comparison stress plots through the thickness for different porosity and graphene platelet distribution types and boundary conditions ($\phi = 60^\circ$ and $L/h = 5$; $c_p = 0.5$; $W_{gpl} = 1\%$): (a) shear stress, (b) normal stress.

Figure 8. Non - dimensional deflections of curved beam ($\phi = 90^\circ$) against GPLs weight fraction (W_{gpl}) for different values of GPL geometry, $(\ell/w)_{gpl}$ & $(\ell/t)_{gpl}$ and boundary conditions ($L/h=5$, $c_p = 0.5$; symmetric distribution type for Porosity and GPLs).

Figure 9. Non - dimensional critical buckling loads of curved beams with different beam angles (ϕ) against GPL weight fraction (W_{gpl}) for different thickness ratios and boundary conditions ($c_p = 0.5$, symmetric distribution type for porosity and GPLs).

Figure 10. Mode shapes (u_0 and w_0) corresponding to the first buckling mode for different beam angles ($c_p = 0.5$, $W_{gpl}=1\%$, symmetric distribution type for porosity and GPLs). a) H – H boundary condition; b) C – C boundary condition

Figure 11. Fundamental frequencies of curved beams with different beam angles (ϕ) against GPL weight fractions (W_{gpl}) for different thickness ratios and boundary conditions ($c_p = 0.5$, symmetric distribution type for porosity and GPLs).

Figure 12. Mode shape (u_0 and w_0) corresponding to the fundamental free vibration mode for different beam angles ($c_p = 0.5$, $W_{gpl}=1\%$, symmetric distribution type for porosity and GPLs). a) H – H boundary condition; b) C – C boundary condition

Table 1. Mesh convergence table for different loading and boundary conditions, C - C and H - H-movable ($L/h=5$, $\phi = 60^\circ$, $c_p = 0.5$, $W_{gpl} = 1\%$).

No. of elements	\bar{u}_3		$\bar{\omega}_1$		P_{cr}	
	C - C	H - H	C - C	H - H	C - C	H - H
2	0.1741	0.2540	28.9013	22.7054	53.5886	38.9586
4	0.1701	0.2534	28.5536	22.6451	46.2255	33.9416
8	0.1706	0.2534	28.4374	22.6361	45.7590	33.7491
16	0.1708	0.2534	28.4055	22.6354	45.7070	33.7357
32	0.1709	0.2534	28.3989	22.6354	45.7022	33.7348
64	0.1709	0.2534	28.3981	22.6354	45.7018	33.7347

Table 2. Comparison of nondimensional deflections (\bar{u}_3) for different L/h , beam angles (ϕ), and theories ($c_p = 0$, $W_{gpl} = 0\%$).

L/h	ϕ	(\bar{u}_3) REF. [67]			(\bar{u}_3) Present		
		CLT	FSDT	SIN	CLT	FSDT	SIN
5	30°	1.0871	1.1800	1.1982	1.0871	1.1800	1.1982
	60°	1.3040	1.4152	1.4370	1.3040	1.4152	1.4370
	90°	1.8401	1.9962	2.0269	1.8401	1.9962	2.0268
10	30°	1.0863	1.1096	1.1142	1.0863	1.1096	1.1142
	60°	1.3005	1.3283	1.3338	1.3005	1.3283	1.3338
	90°	1.8288	1.8678	1.8756	1.8288	1.8678	1.8756
20	30°	1.0862	1.0920	1.0931	1.0862	1.0920	1.0920
	60°	1.2996	1.3065	1.3079	1.2996	1.3065	1.3079
	90°	1.8260	1.8358	1.8377	1.8260	1.8357	1.8376

Table 3. Comparison of non-dimensional first, second and third fundamental frequencies of curved isotropic beam (H - H-movable boundary condition, $\phi = 60^\circ$).

L/h	Mode	Present			Hosseini <i>et al.</i> [66]	
		CLT	FSDT	SIN	Sol ⁿ I	Sol ⁿ II
10	$\bar{\omega}_1$	8.2864	8.2004	8.1837	8.1991	8.2152
	$\bar{\omega}_2$	37.2371	35.8230	35.5630	35.7451	35.8144
	$\bar{\omega}_3$	84.1010	77.7885	76.7076	77.3993	77.5359
50	$\bar{\omega}_1$	8.3213	8.3178	8.3171	8.3177	8.3184
	$\bar{\omega}_2$	37.8341	37.7697	37.7569	37.7658	37.7690
	$\bar{\omega}_3$	87.0629	86.7317	86.6665	86.7084	86.7158

Table 4. Critical buckling load, \bar{P}_{cr} , of an isotropic curved beam (H - H-movable)

Critical buckling load (\bar{P}_{cr})	Method	Value
Present	FEA	37.37
Luu et al. [64]	IGA	39.40
Timoshenko and Gere [65]	Exact	38.38
Kang et al. [68]	DQM	38.49

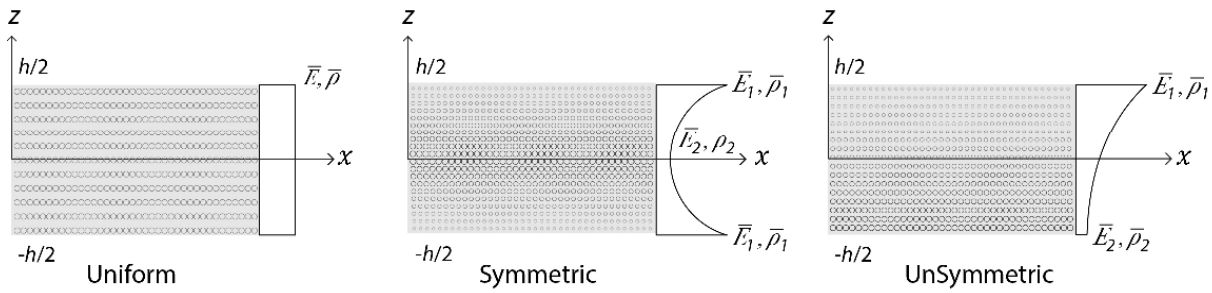
Table 5. Non-dimensional deflection (\bar{u}_3) of curved beams of different porosity and GPLs weight distribution types for different boundary conditions ($c_p = 0.5$, $W_{gpl} = 1\%$).

L/h	ϕ	Porosity Dist. Type	\bar{u}_3 (H – H)			\bar{u}_3 (C – H)			\bar{u}_3 (C – C)		
			GPL Dist. Type			GPL Dist. Type			GPL Dist. Type		
			Sym.	Unsym.	Uniform	Sym.	Unsym.	Uniform	Sym.	Unsym.	Uniform
5	Straight	Sym.	0.7946	0.9117	0.9334	0.4235	0.4815	0.4688	0.2706	0.2955	0.2849
		Unsym.	0.8824	0.9982	1.0587	0.4647	0.5467	0.5273	0.2881	0.3292	0.3117
		Uniform	0.9134	1.0703	1.1004	0.4656	0.5423	0.5321	0.2866	0.3215	0.3124
	45°	Sym.	0.3579	0.3208	0.3894	0.2656	0.2676	0.2869	0.2031	0.2219	0.2135
		Unsym.	0.3257	0.3098	0.3559	0.2658	0.2738	0.2893	0.2169	0.2407	0.2308
		Uniform	0.3893	0.3492	0.4185	0.2871	0.2907	0.3116	0.2150	0.2376	0.2298
10	Straight	Sym.	0.6924	0.8234	0.8478	0.3155	0.3883	0.3776	0.1745	0.2120	0.2037
		Unsym.	0.7898	0.9191	0.9815	0.3668	0.4640	0.4449	0.2007	0.2544	0.2381
		Uniform	0.8216	0.9915	1.0238	0.3679	0.4586	0.4500	0.1997	0.2464	0.2392
	45°	Sym.	0.1316	0.1233	0.1400	0.1139	0.1146	0.1238	0.0942	0.1065	0.1040
		Unsym.	0.1240	0.1219	0.1320	0.1139	0.1156	0.1229	0.1033	0.1152	0.1130
		Uniform	0.1409	0.1316	0.1463	0.1238	0.1234	0.1322	0.1036	0.1159	0.1136

Table 6. Non-dimensional buckling load, \bar{P}_{cr} of different porosity and GPLs weight distribution types for different boundary conditions ($c_p = 0.5$, $W_{gpl} = 1\%$).

L/h	ϕ	Porosity Dist. Type	$\bar{P}_{cr} (H - H)$			$\bar{P}_{cr} (C - H)$			$\bar{P}_{cr} (C - C)$		
			GPL Dist. Type			GPL Dist. Type			GPL Dist. Type		
			Sym.	Unsym.	Uniform	Sym.	Unsym.	Uniform	Sym.	Unsym.	Uniform
5	Straight	Sym.	12.7509	11.1354	10.8551	21.5291	18.7961	19.2864	33.7904	30.6660	31.8268
		Unsym.	11.4974	10.2003	9.5803	19.5156	16.4880	17.0643	31.5406	27.3215	28.9035
		Uniform	11.0922	9.4837	9.2077	19.4633	16.5927	16.8921	31.7123	28.0159	28.8442
	45°	Sym.	29.2827	30.6251	26.9201	32.0643	31.8196	29.6735	42.2129	39.4165	40.4182
		Unsym.	31.5053	27.2662	28.8727	32.0253	30.8646	29.3272	40.1783	36.5079	37.7502
		Uniform	26.9290	27.9801	25.0513	29.6730	29.1803	27.1097	40.0895	36.7652	37.4818
10	Straight	Sym.	14.6324	12.3327	11.9513	28.2040	22.8551	23.4641	51.0039	41.7201	43.4204
		Unsym.	12.8465	11.0829	10.3351	24.2030	19.1255	19.8820	44.1466	34.6224	37.0038
		Uniform	12.3324	10.2395	9.8967	24.1082	19.2999	19.6352	44.3690	35.7556	36.8310
	45°	Sym.	50.9782	41.6773	43.3986	60.3205	54.5715	53.2042	83.4023	73.7898	75.3282
		Unsym.	44.1065	34.5757	36.9728	56.5342	47.5889	48.7154	76.2413	64.3994	68.4848
		Uniform	44.3467	35.7215	36.8124	53.8630	47.6591	46.6072	75.7490	66.2759	67.9921

a) Porosity Distribution types



b) GPL Distribution types

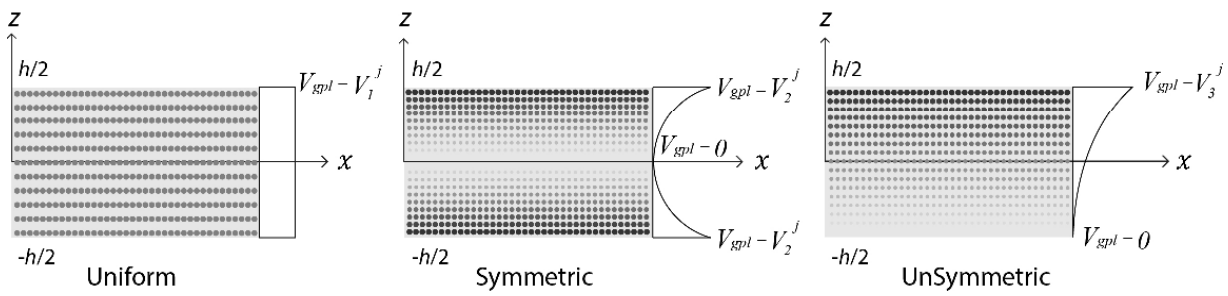


Figure 1. Distribution of porosity and GPLs in the thickness direction: (a) Porosity; (b) GPLs.

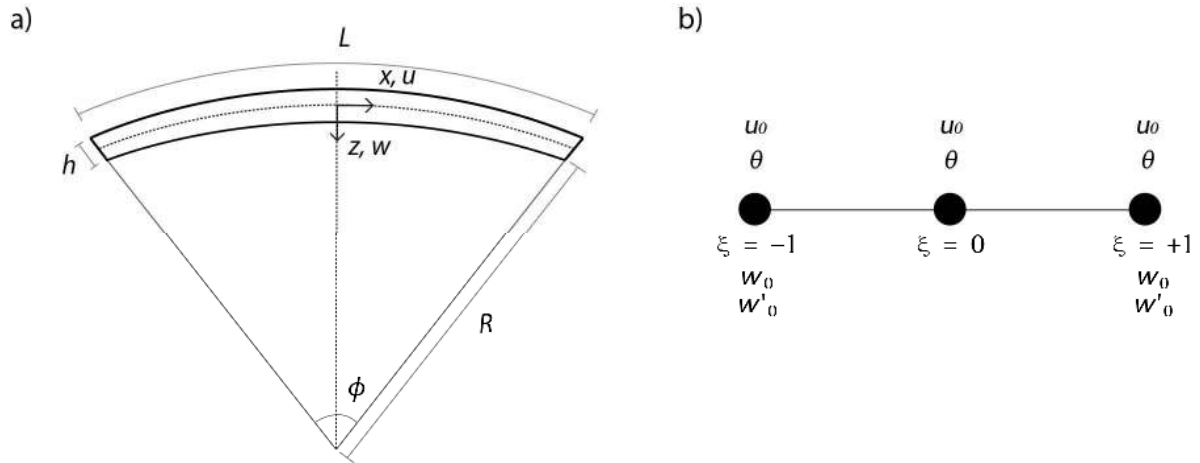


Figure 2. a) Geometrical parameters of curved beam & b) Beam element with the degrees of freedom.

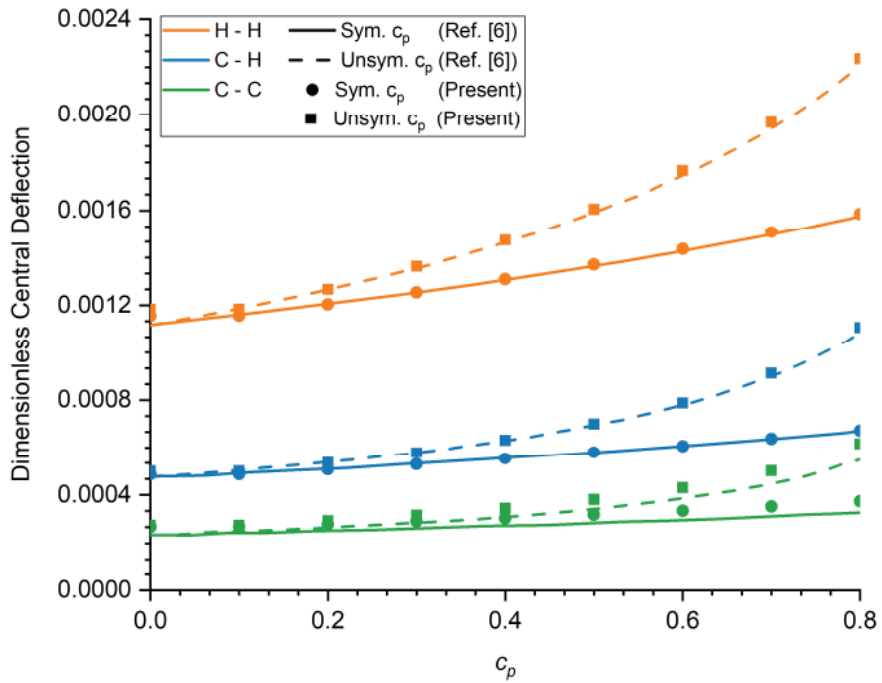


Figure 3. Comparison of non - dimensional deflections against porosity coefficient for the straight nanocomposite beam under uniform load for different boundary conditions ($L/h = 20$, $W_{gpl} = 0\%$).

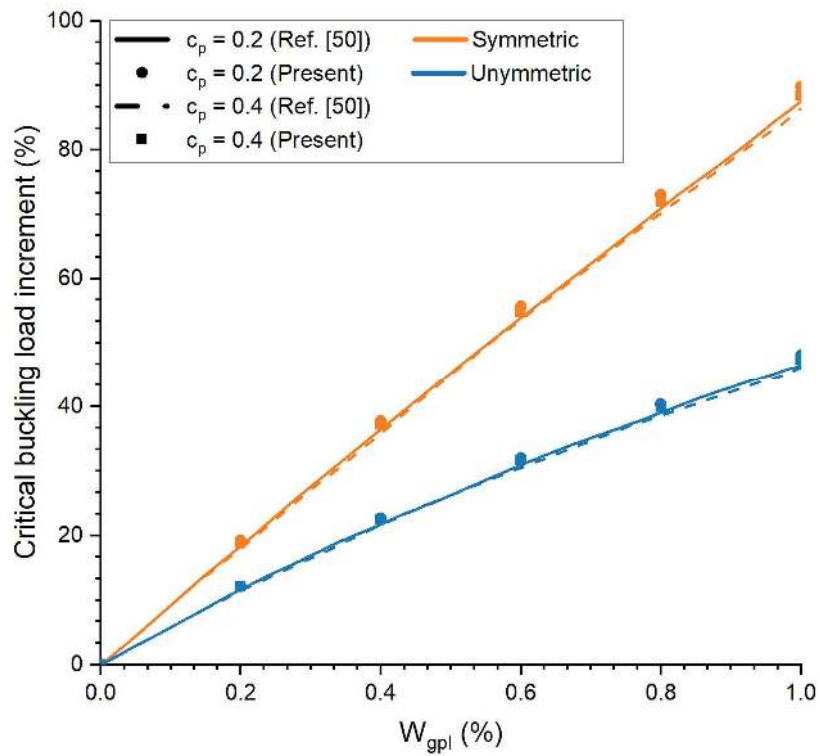


Figure 4. Comparison of critical buckling load increment of straight GPL reinforced beam against weight fraction of GPL for different values for porosity coefficient and different GPL distributions (C - C boundary condition, $L/h=20$, symmetric porosity distribution).

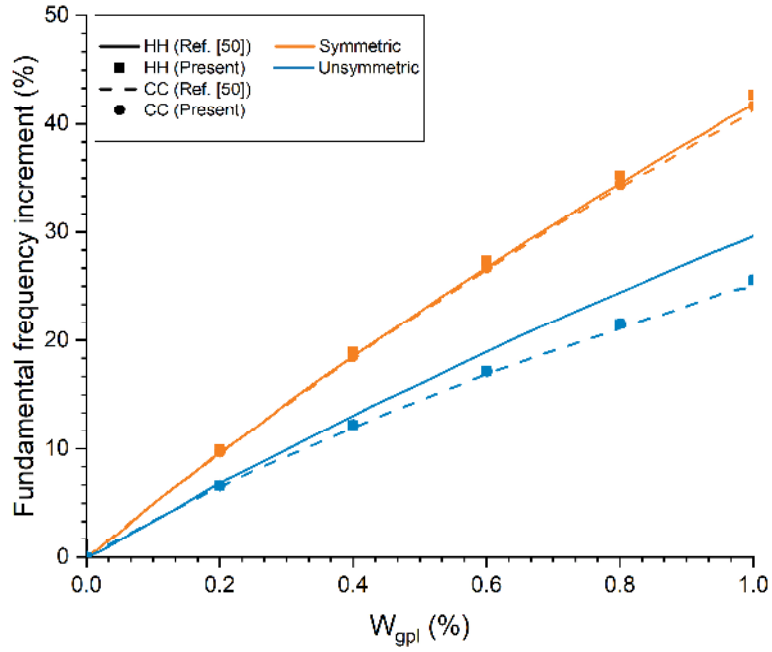


Figure 5. Comparison of fundamental frequency increment of straight GPL reinforced beam against weight fraction of GPLs for different GPL distributions and boundary conditions ($c_p = 0.5$, $L/h = 20$, symmetric porosity distribution).

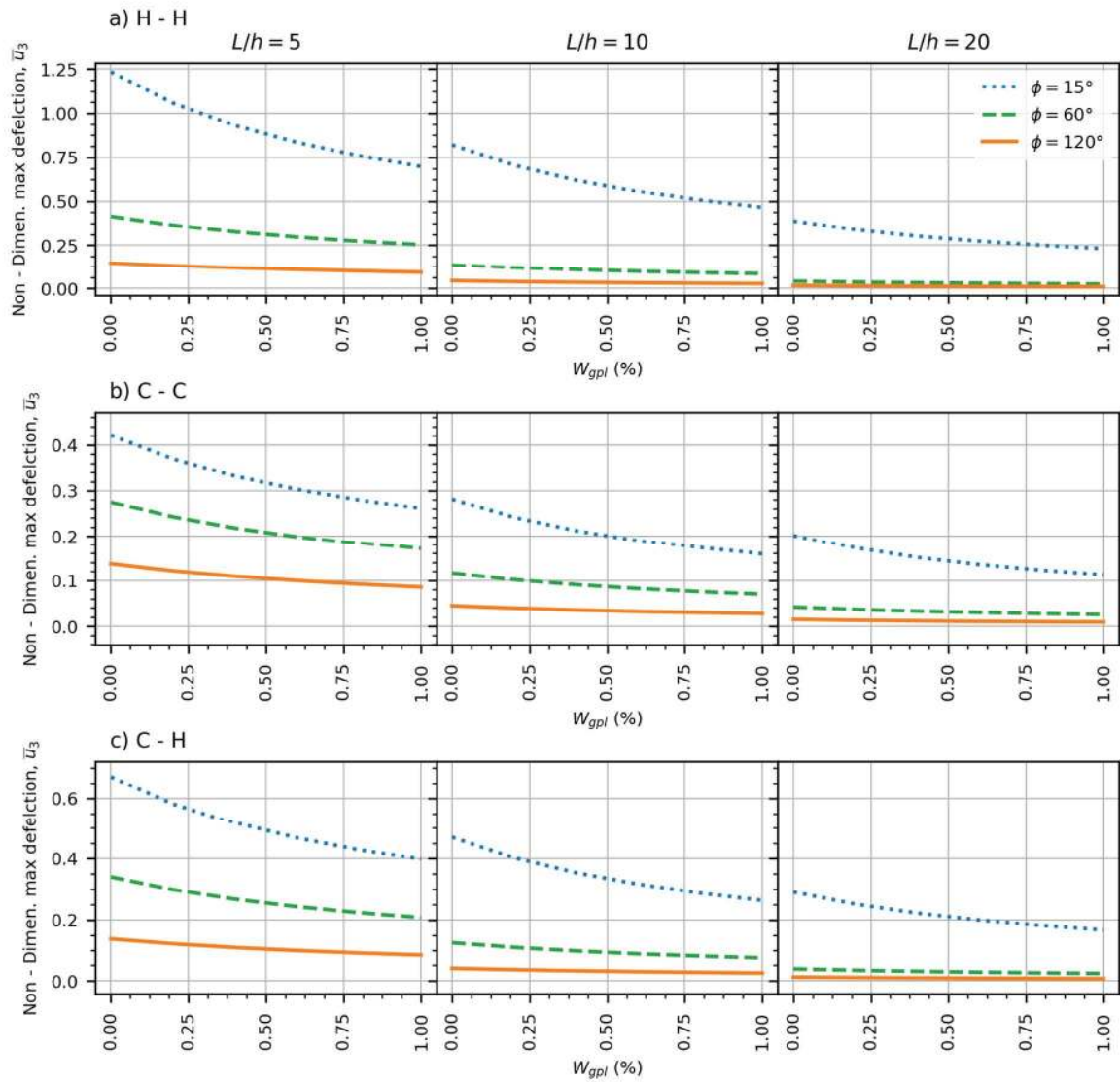


Figure 6. Non - dimensional deflections of curved beams with different beam angles (ϕ) against GPL weight fraction (W_{gpl}) for different thickness ratios and different boundary conditions ($c_p = 0.5$, symmetric distribution type for porosity and GPLs).

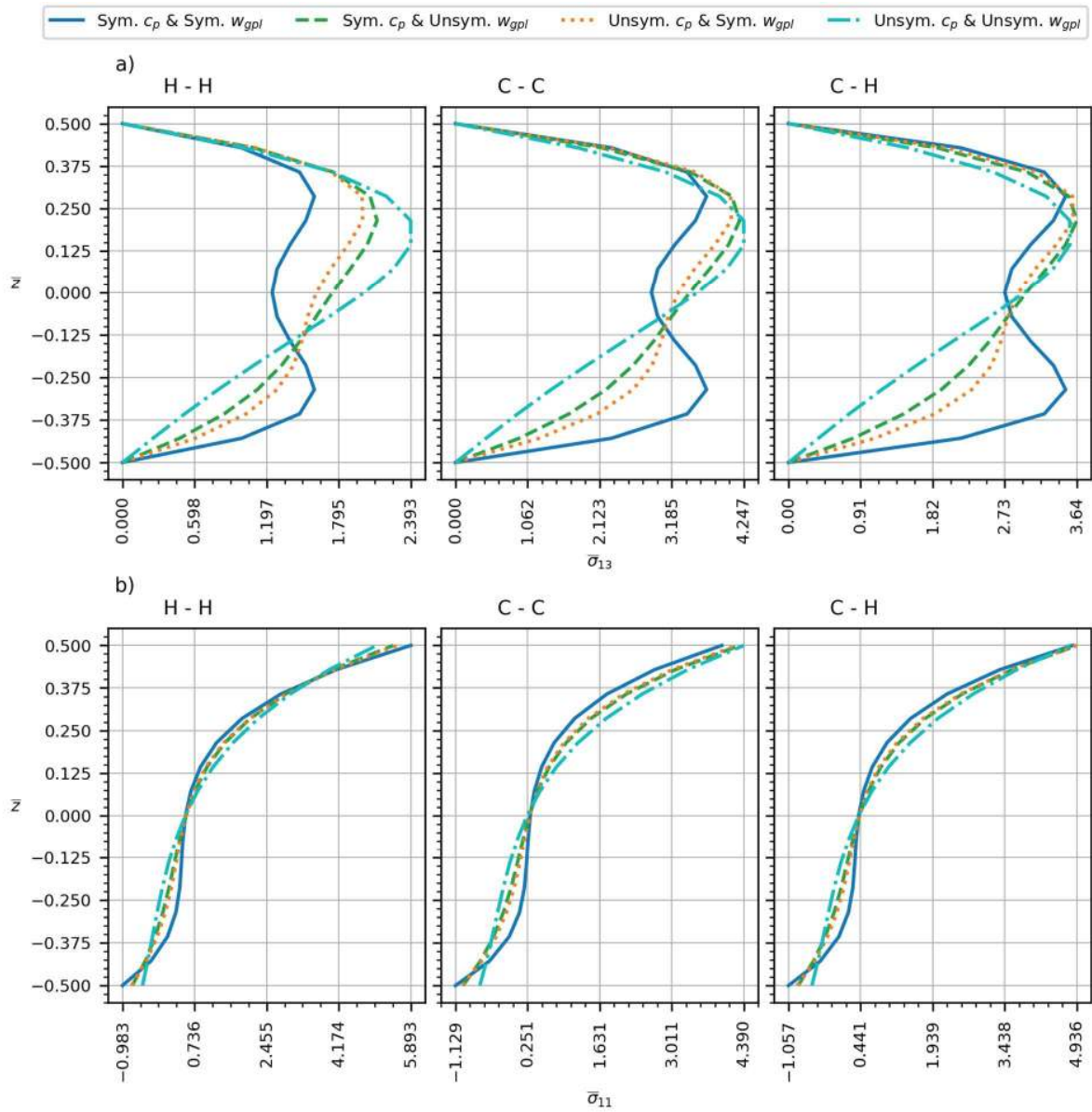


Figure 7. Comparison stress plots through the thickness for different porosity and graphene platelet distribution types and boundary conditions ($\phi = 60^\circ$ and $L/h = 5$; $c_p = 0.5$; $W_{gpl} = 1\%$): (a) shear stress, (b) normal stress.

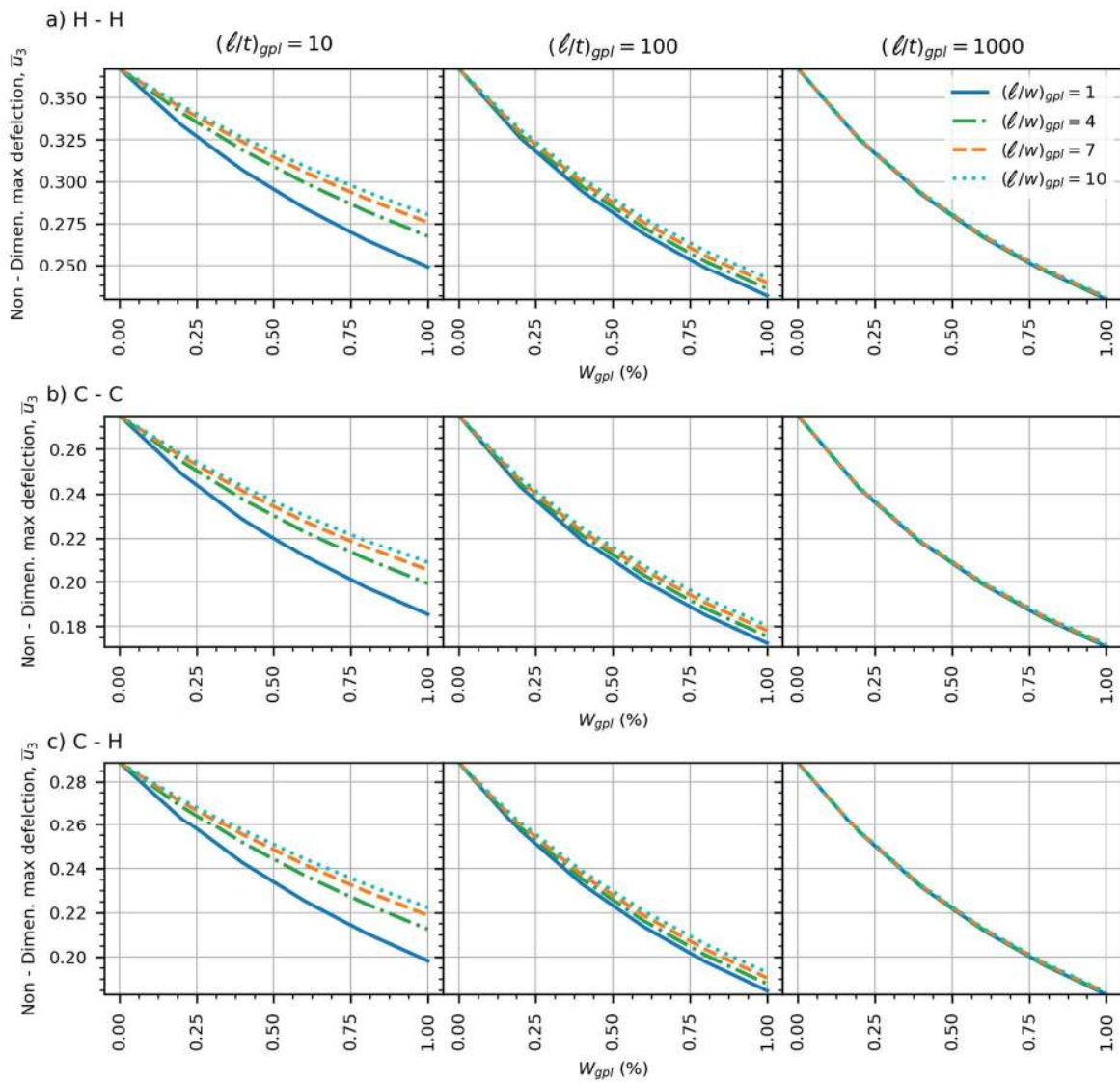


Figure 8. Non - dimensional deflections of curved beam ($\phi = 90^\circ$) against GPLs weight fraction (W_{gpl}) for different values of GPL geometry, $(\ell/w)_{gpl}$ & $(\ell/t)_{gpl}$ and boundary conditions ($L/h=5$, $c_p = 0.5$; symmetric distribution type for Porosity and GPLs).

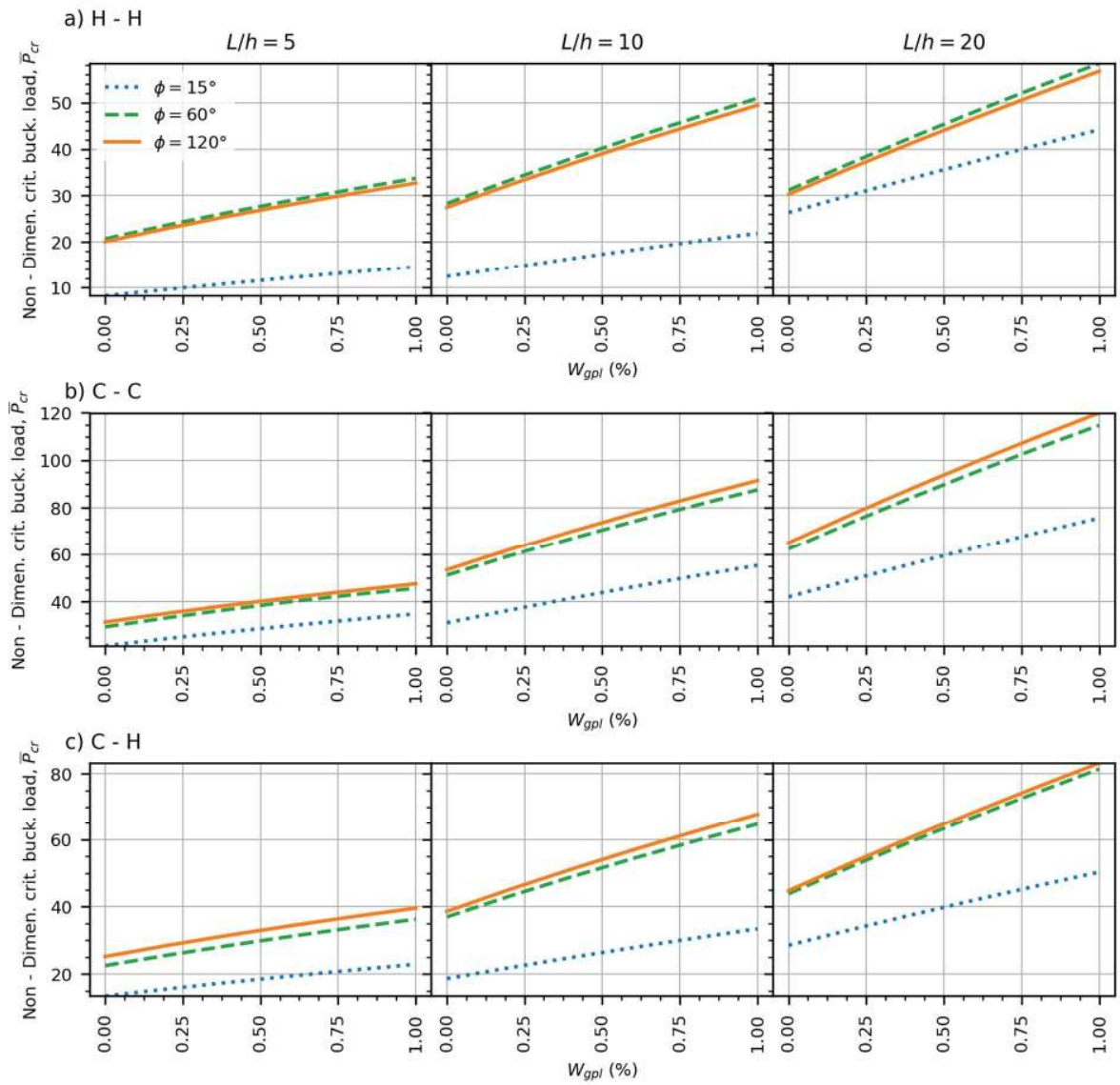


Figure 9. Non - dimensional critical buckling loads of curved beams with different beam angles (ϕ) against GPL weight fraction (W_{gpl}) for different thickness ratios and boundary conditions ($c_p = 0.5$, symmetric distribution type for porosity and GPLs).

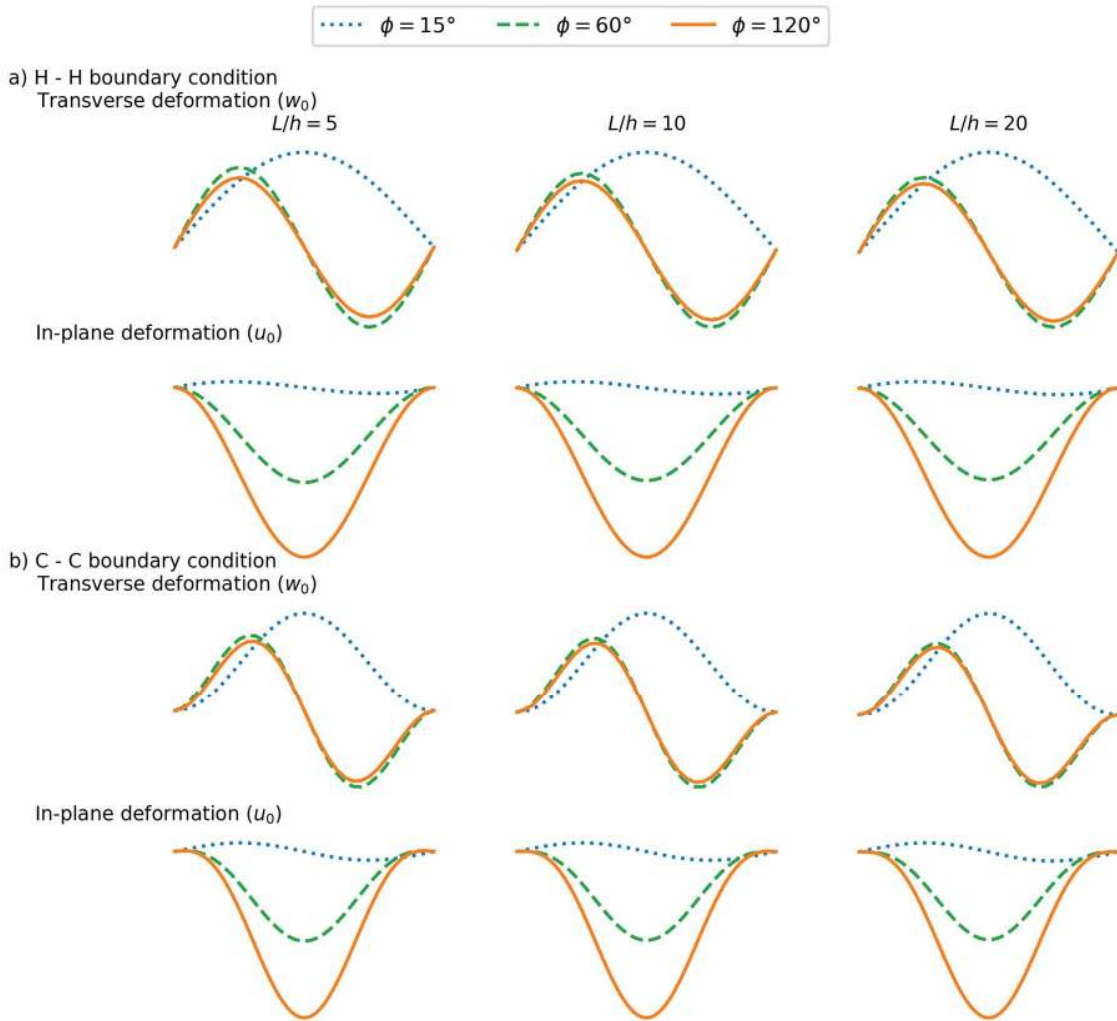


Figure 10. Mode shapes (u_0 and w_0) corresponding to the first buckling mode for different beam angles ($c_p = 0.5$, $W_{gp} = 1\%$, symmetric distribution type for porosity and GPLs). a) H – H boundary condition; b) C – C boundary condition

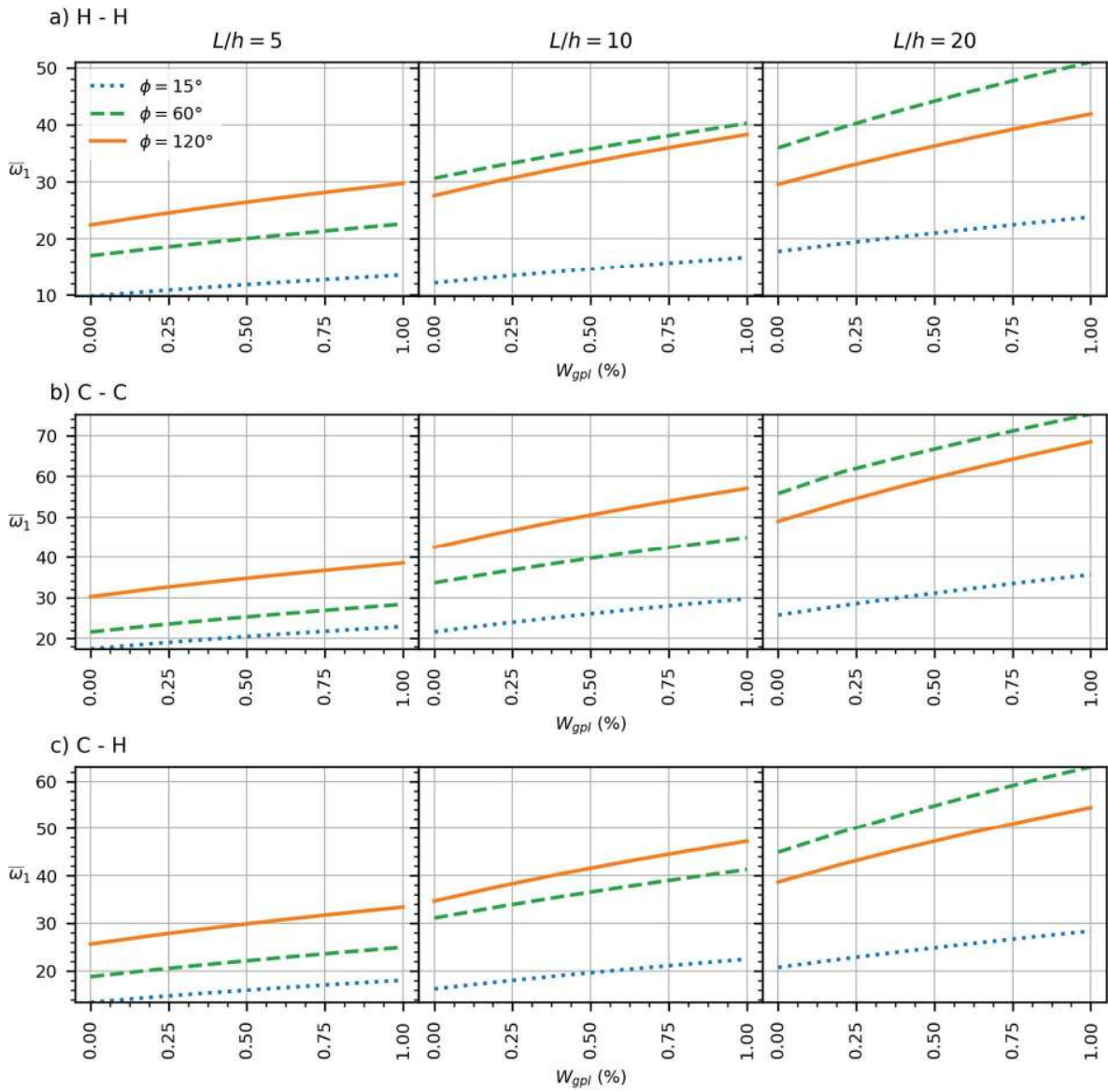


Figure 11. Fundamental frequencies of curved beams with different beam angles (ϕ) against GPL weight fractions (W_{gpl}) for different thickness ratios and boundary conditions ($c_p = 0.5$, symmetric distribution type for porosity and GPLs).

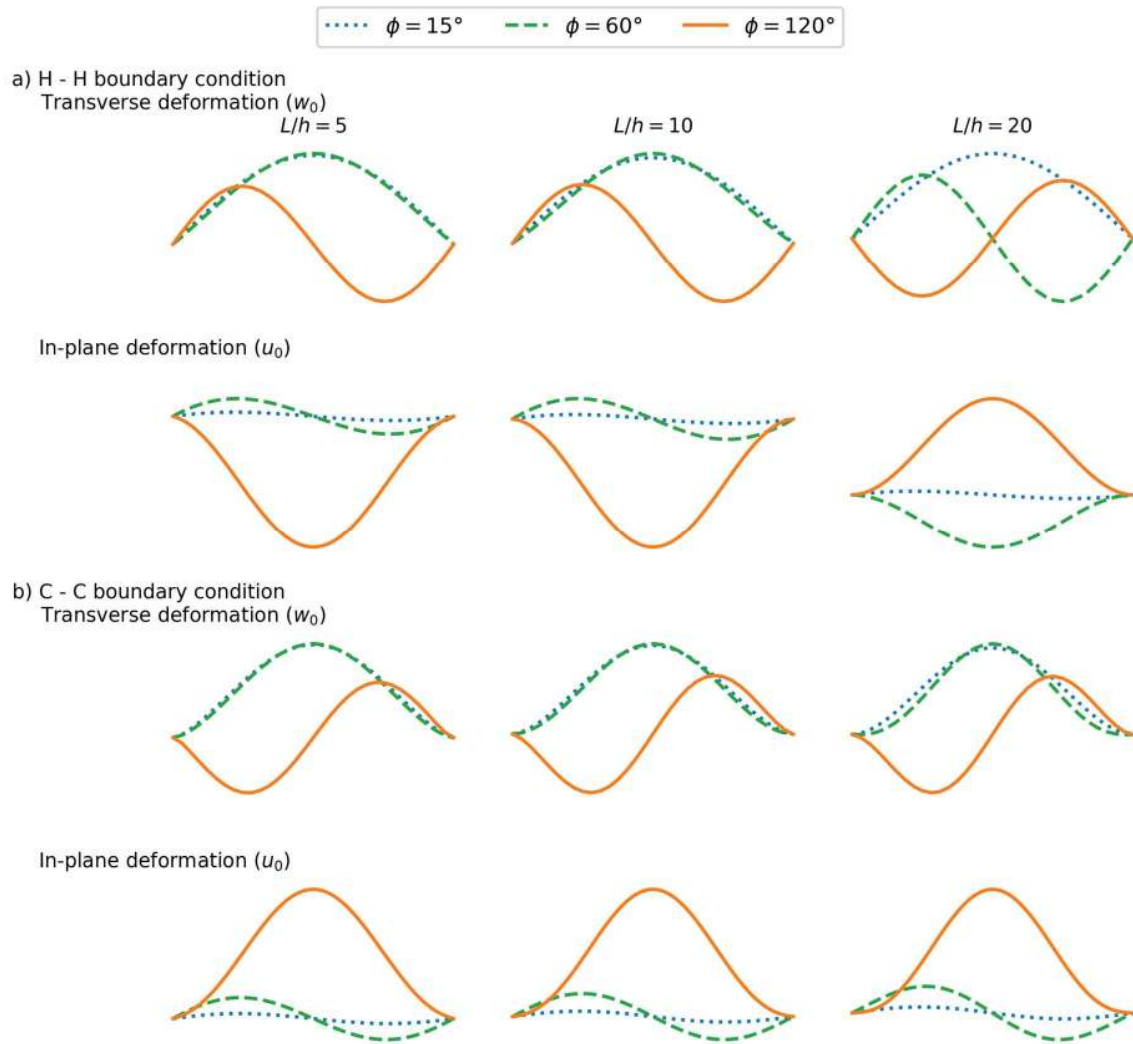


Figure 12. Mode shape (u_0 and w_0) corresponding to the fundamental free vibration mode for different beam angles ($c_p = 0.5$, $W_{GPL}=1\%$, symmetric distribution type for porosity and GPLs). a) H – H boundary condition; b) C – C boundary condition